

Technische Universität Dresden • Faculty of Mathematics

# Derivation and study of a non-confluent model for deformable cells

Master's thesis

to obtain the second degree

*Master of Science*  
(*M.Sc.*)

written by

TIM VOGEL

(born on June 9, 2002 in FINSTERWALDE)

Day of submission: November 4, 2025

Supervised by Jun.-Prof. Dr. Markus Schmidtchen  
(Institute of Scientific Computing)

# Contents

<b>1</b>	<b>Introduction</b>	<b>5</b>
1.1	Review of cell model literature . . . . .	7
1.2	Thesis overview . . . . .	24
<b>2</b>	<b>DF model validation and simulation analysis</b>	<b>25</b>
2.1	Reference simulations: Bruna and Chapman (2012) . . . . .	25
2.2	Reproduction of reference results . . . . .	28
2.3	Shape deformation check . . . . .	28
<b>3</b>	<b>Density computations</b>	<b>34</b>
3.1	Transition $\mu^{N_C} \xrightarrow{N_C \rightarrow \infty} \mu$ . . . . .	35
3.2	General energy computation . . . . .	35
<b>4</b>	<b>Conclusion</b>	<b>37</b>
<b>5</b>	<b>Outlook</b>	<b>38</b>

## Nomenclature

abbreviation	description
PDE	A partial differential equation is an equation that contains unknown multivariable functions and their partial derivatives.
SDE	A stochastic differential equation is a differential equation in which one or more of the terms is a stochastic process, resulting in a solution that is also a stochastic process.
DF model	The discrete form model is a vertex cell model that is defined by a list of all wall points.

# Mathematical conventions

symbol	description
$\vec{v}$	Superscript arrows denote multidimensional variables
$\frac{\partial f}{\partial v}$	Partial derivative of a scalar function $f$ with respect to a one dimensional variable $v$
$\nabla_{\vec{v}} f$	Gradient $\nabla_{\vec{v}} f = (\frac{\partial f}{\partial v_1}, \dots, \frac{\partial f}{\partial v_n})^T$ , where $f$ is a scalar function and $\vec{v} = (v_1, \dots, v_n)^T$ is a multidimensional variable
$\nabla_{\vec{v}} \cdot F$	Divergence $\nabla_{\vec{v}} \cdot F = \frac{\partial F_1}{\partial v_1} + \dots + \frac{\partial F_n}{\partial v_n}$ , where $F = (F_1, \dots, F_m)^T$ is a vector valued function
$D_{\vec{v}} F$	Jacobian matrix $D_{\vec{v}} F = \begin{pmatrix} \frac{\partial F_1}{\partial v_1} & \dots & \frac{\partial F_1}{\partial v_n} \\ \vdots & & \vdots \\ \frac{\partial F_m}{\partial v_1} & \dots & \frac{\partial F_m}{\partial v_n} \end{pmatrix}$ ,
$\Delta f$	Laplacian of a scalar function $f$
$2e - 3$	Scientific notation for $2 \times 10^{-3} = 0.002$
$d\vec{B}_i(t)$	Two dimensional Brownian motion applied to cell $i$ at time $t$ in SDEs
$I_d$	Identity matrix in $\mathbb{R}^{d \times d}$
$\mathbb{R}_+$	Positive real numbers including 0, i.e. $[0, \infty)$
$\mathbb{N}$	Natural numbers excluding 0
$\mathbb{N}_0$	Natural numbers including 0
$N_C \in \mathbb{N}$	Number of cells in a model
$N_V \in \mathbb{N}$	Number of vertices of each cell in a model
$P(t; \vec{x}_1, \dots, \vec{x}_{N_C})$	Joined probability density function
$\rho(t; \vec{x})$	First marginal function

# 1 Introduction

Collective cell migration represents a fundamental process underpinning various biological phenomena, including embryonic development, tissue regeneration, wound healing, and the invasive potential of certain cancers. The collective nature of cell movement has been acknowledged for over a century, with early observations recognising its importance in developmental and regenerative processes [AT20, Hol14, Her32, VT66]. However, the underlying mechanisms driving this coordinated behaviour remained contentious, with competing hypotheses suggesting roles for pressure [Her32], surface tension [AT20], or active forces generated by leading cells [Hol14]. Following a period where research emphasis shifted towards molecular and genetic details, the field has witnessed a resurgence of interest in understanding the physical principles governing collective cell migration. This revival is largely attributed to recent advances in experimental techniques [RCCT17, DRSB<sup>+</sup>05, TWA<sup>+</sup>09], enabling direct measurements of mechanical forces exerted by cells, and the development of new conceptual frameworks in biophysics and active matter physics [MJR<sup>+</sup>13, PJJ15, JGS18], which challenged purely reductionist perspectives [GT18]. These developments coincided with a growing recognition of the critical role of collective cell migration not only in physiological processes but also in the progression of malignant diseases [FNW<sup>+</sup>95].

The diverse manifestations of collective cell migration depend heavily on the specific biological context and tissue type [FG09]. For instance, epithelial cells often migrate as cohesive sheets on the extracellular matrix (ECM) during morphogenesis, wound closure, and regeneration. Snapshots from a cell wound healing process, illustrating the dynamics of cell migration, are shown in Figure 1.

In contrast, cancer cells often invade tissues as sheets, strands, or clusters, navigating a complex three-dimensional extracellular matrix (ECM) environment [FG09, CCP<sup>+</sup>14, CV15].

While cell migration occurs extensively in three dimensions, modelling these complex processes remains a significant challenge. Consequently, much current scientific work focuses on two dimensional systems as a more tractable approach to understand the underlying physical principles.

Throughout this thesis, we study cell dynamics in a bounded two dimensional domain  $\Omega \subset \mathbb{R}^2$ . The domain is taken to be a square centred at the origin with side length  $2L$ , where  $L > 0$ , and is defined as

$$\Omega = [-L, L]^2.$$

In this work, the total number of cells present within the domain  $\Omega$  is denoted by  $N_C \in \mathbb{N}$ .

In two dimensions, cell monolayers serve as fundamental model systems to study cell behaviour and tissue function. These systems, comprising a single layer of cells grown on a surface, can be mathematically and computationally modelled in either a confluent or non-confluent manner. A confluent cell model depicts a continuous, tightly packed layer where cells cover the entire surface without gaps, whereas a non-confluent monolayer represents a state with spaces and gaps between individual cells or cell clusters that have not yet achieved full surface coverage.



`figures/intro/cell-migration.pdf`

Figure 1: A figure from the paper [AT20] illustrating cell migration during the wound healing process. (a) Vector field representation of cellular traction forces in cells as they close a wound, with color intensity reflecting the radial component (positive values indicate outward-directed forces). Panels labelled i and ii present magnified views of the regions marked by arrows in panel (a). (b) Velocity vectors (green) and monolayer stress ellipses (red), depicting the principal stress directions and magnitudes, in a growing cell colony (phase contrast).

Recent years have seen growing interest in understanding the principles governing collective cell migration in confluent cell monolayers and epithelial tissues, which exhibit remarkable patterns and correlations in both structural arrangements and actively driven flows [WV21]. Experimental studies on model systems have revealed phenomena such as unjamming transitions, spontaneous vortex formation, topological defects, and active turbulence. A key challenge is linking this macroscopic behaviour to the properties of individual cells and their interactions, leading to a diverse range of modelling approaches spanning different levels of coarse-graining, from subcellular lattices and multiphase field models to vertex, Voronoi, particle, and continuum models. The systematic comparison of these diverse cell models is crucial for selecting appropriate methods for future studies and enabling predictive simulations of patterns and correlations in cell colonies.

Understanding the collective behaviour of cells, particularly in processes such as wound healing, tissue regeneration, and embryonic development, is a central challenge in computational and mathematical biology. These phenomena arise from the interplay of intrinsic cell dynamics and extrinsic cues, including chemical gradients,

mechanical forces, and the physical constraints of the environment. A key aspect of this behaviour is the diffusion-like motion of cells, which governs how populations spread, organize, and respond to perturbations.

To gain insight into these processes, we focus on the diffusion dynamics of cells as a fundamental tool for characterizing and comparing different modelling approaches. In this thesis, we investigate how distinct mathematical cell models, ranging from point particles to extended, deformable cells, give rise to different diffusion behaviours. By analysing the underlying mechanisms that drive cell movement and spatial spreading, we aim to uncover the role of cell shape, interaction dynamics, and mechanical properties in shaping collective migration patterns, ultimately providing a deeper understanding of biological processes such as wound closure and tissue morphogenesis.

## 1.1 Review of cell model literature

Each cell model employs distinct dynamical rules and interaction mechanisms, leading to qualitatively and quantitatively different diffusion behaviours. These differences arise from how the models represent cell shape, internal structure, cell-cell interactions, and response to external cues. As a result, the emergent collective dynamics, such as the speed of spreading, the formation of clusters or gaps, and the sensitivity to crowding, can vary significantly across models.

To establish a comprehensive understanding of these variations, we now provide an overview of the most widely used cell modelling approaches. Starting from the simplest representation, we progress through increasingly complex frameworks, highlighting their underlying assumptions, mathematical structure, and implications for cell diffusion. This comparative analysis sets the foundation for our investigation into how model-specific dynamics influence the macroscopic behaviour of cell populations.

### Point particle model

We consider the point particle model on the square  $\Omega \subset \mathbb{R}^2$ , where  $N_C$  point particles are located in. Initially, these particles are randomly distributed in  $\Omega$ . We impose the reflective boundary condition on  $\partial\Omega$ .

Let

$$\vec{x}_i(t) \in \Omega, \quad 1 \leq i \leq N_C,$$

be the location of the particle  $i$  at time  $t > 0$ . In this model, cells are considered to be point particles with no real size. There is also no particle interaction, as there is no possibility of collision.

The particles' dynamics are governed solely by Brownian motion. Brownian motion is a random and unpredictable motion that occurs in the real world when particles are suspended in a fluid and collide with surrounding molecules.

In mathematics, we model Brownian motion using stochastic differential equations (SDEs), which are equations that describe the motion of a particle over time in a random and unpredictable manner. SDEs are a powerful tool for modelling complex phenomena in physics, finance, and other fields, and are characterized by the

presence of random terms that capture the uncertainty of the system.

The particle movement can be modelled using the following SDE, which describes the random motion of particles over time

$$d\vec{x}_i(t) = \sqrt{2D} d\vec{B}_i(t), \quad 1 \leq i \leq N_C,$$

where the constant  $D > 0$  represents the diffusion coefficient which proportionally scales the speed of the particle movements by scaling the random fluctuations.

The term  $d\vec{B}_i(t)$  represents the stochastic increment of a two dimensional Wiener process (Brownian motion) associated with particle  $i$ . It models the random, unpredictable fluctuations in the particle's position over time.

For infinitesimally small time intervals  $dt$ , the increment  $d\vec{B}_i(t)$  is normally distributed with mean zero and covariance  $dt \cdot I_2$ , where  $I_2$  denotes the  $2 \times 2$  identity matrix.

This dynamic is fundamental and widely used in SDEs across various fields, including modelling particle diffusion [BC12], biological systems such as cell migration and also financial markets.

The stochastic dynamics of individual particles—governed by Brownian motion and external forces—naturally give rise to a probability density function that characterises the collective behaviour of the entire system through a mean field description. This density function serves as the fundamental mean field that encapsulates the averaged influence of all particles, enabling a seamless transition from microscopic particle trajectories to a macroscopic description of cell distribution where individual fluctuations are replaced by deterministic evolution of the ensemble density.

When analysing the diffusion behaviour of a cell model, our focus shifts to understanding the evolution of this density. The first marginal density function  $\rho(t; \vec{x})$  serves as a central quantity in this analysis, representing the probability of finding any particle at position  $\vec{x} \in \Omega$  and time  $t > 0$ . It provides a coarse grained view of the system, capturing how the spatial distribution of cells evolves over time and revealing key features of collective migration, such as spreading rates and pattern formation.

In order to compute the first marginal, we have to start with the joint probability density function. This function, denoted by

$$\begin{aligned} P : \mathbb{R}_+ \times \Omega^{N_c} &\longrightarrow \mathbb{R}_+, \\ (t; \vec{x}_1, \dots, \vec{x}_{N_C}) &\longmapsto P(t; \vec{x}_1, \dots, \vec{x}_{N_C}). \end{aligned}$$

$P(t; \vec{x}_1, \dots, \vec{x}_{N_C})$  tells the probability that the whole cell configuration is in the given state  $\vec{x}_1, \dots, \vec{x}_{N_C} \in \Omega$  at time  $t$ . It is defined on the high dimensional configuration space  $\mathbb{R}_+ \times (\Omega)^{N_c} \subset \mathbb{R} \times (\mathbb{R}^2)^{N_c}$  and fulfils

$$\int_{\Omega^{N_C}} P(t; \vec{x}_1, \dots, \vec{x}_{N_C}) d\vec{x}_1 \dots d\vec{x}_{N_C} = 1,$$

for all  $t > 0$ .

We define  $\vec{X} = (\vec{x}_1, \dots, \vec{x}_{N_C})^T$ . The derivation of the high dimensional diffusion equation is based on the principle of probability conservation in the configuration

space. Starting from the stochastic dynamics of  $N_C$  independent particles undergoing pure Brownian motion, the evolution of the joint probability density  $P(t; \vec{X})$  is governed by the continuity equation, which states that the rate of change of probability within a region is equal to the net flux of probability across its boundary.

In the absence of external forces, the probability flux is purely diffusive, proportional to the gradient of  $P$ , with diffusion coefficient  $D$ .

Applying the divergence theorem in the  $2N_C$  dimensional configuration space  $\Omega^{N_C}$ , the surface integral of the flux is converted into a volume integral, leading to the Laplacian operator acting on  $P$ . This results in the final form of the equation:

$$\frac{\partial P}{\partial t} = D\Delta_{\vec{X}}P, \quad \vec{X} \in \Omega^{N_C}, \quad t > 0,$$

where  $D$  is the diffusion constant from the particle dynamic and  $\Delta_{\vec{X}}$  is the Laplacian operator with respect to  $\vec{X}$ .

Having obtained the joint probability function  $P(t; \vec{X})$ , we can continue by deriving the first marginal  $\rho(t; \vec{x})$ . In contrast to the joint probability function that tells probabilities of a whole cell configuration  $\vec{X}$ , the first marginal function is a probability density that describes the likelihood of finding any one particle at position  $\vec{x} \in \Omega$  and time  $t > 0$ .

The first marginal still fulfils the condition

$$\int_{\Omega} \rho(t; \vec{x}) d\vec{x} = 1, \quad t > 0.$$

We can obtain  $\rho(t; \vec{x})$  by integrating the joint probability density  $P(t; \vec{x}_1, \dots, \vec{x}_{N_C})$  over the positions of all particles except the first, i.e., over  $\vec{x}_2, \dots, \vec{x}_{N_C}$

$$\rho(t; \vec{x}_1) = \int_{\Omega^{N_C-1}} P(t; \vec{X}) d\vec{x}_2 \dots d\vec{x}_{N_C}.$$

This marginalisation process effectively averages out the influence of the other particles, yielding the probability density  $\rho(t; \vec{x})$  for finding any one particle at position  $\vec{x}$ . Due to the indistinguishability of the particles, this marginal is the same for any particle and represents the macroscopic distribution of the system. By integrating out all particles but one, we find  $\rho$  acting on a much lower dimensional space

$$\begin{aligned} \rho : \mathbb{R}_+ \times \Omega &\longrightarrow \mathbb{R}_+, \\ (t; \vec{x}) &\longmapsto \rho(t; \vec{x}_1). \end{aligned}$$

In the setting of our point particle model, the first marginal  $\rho$  satisfies the partial differential equation:

$$\frac{\partial \rho(t; \vec{x})}{\partial t} = D\Delta_{\vec{x}}\rho(t; \vec{x}), \quad \vec{x} \in \Omega, \quad t > 0,$$

where  $\Delta_{\vec{x}}$  is the Laplacian operator with respect to the spatial variables.

This equation represents the classic diffusion equation, a cornerstone of physics and mathematics. The same diffusion constant  $D > 0$  is used in the SDE for particle

movement and the PDE for the probability density function  $\rho$ .

If we wish to model additional dynamics for our point particles - such as directed motion towards a food source or response to a chemical gradient - we must incorporate an external force into the system. This force is modelled by a vector valued function  $f(\vec{x})$ , which depends on the particle's position  $\vec{x}$  and represents the influence of external cues, such as chemotactic gradients or mechanical drag

$$\begin{aligned} f : \Omega &\longrightarrow \mathbb{R}^2, \\ \vec{x} &\longmapsto f(\vec{x}). \end{aligned}$$

This force modifies the stochastic dynamics by introducing a deterministic drift component, enabling the particles to exhibit non-random, directed movement in response to their environment. This yields a new particle dynamic

$$d\vec{x}_i(t) = f(\vec{x}_i(t))dt + \sqrt{2D} d\vec{B}_i(t), \quad 1 \leq i \leq N_C.$$

We define a multidimensional function

$$\begin{aligned} F : \Omega^{N_C} &\longrightarrow (\mathbb{R}^2)^{N_C}, \\ \vec{X} &\longmapsto F(\vec{X}) = (f(\vec{x}_1), \dots, f(\vec{x}_{N_C}))^T, \end{aligned}$$

that gathers the external dynamics for all particles.

With that new external force, the diffusion behaviour changes. For our point particle model with included external effects, the joint probability is given by a high dimensional Fokker-Planck equation

$$\frac{\partial P(t; \vec{X})}{\partial t} = \nabla_{\vec{X}} \cdot [D \nabla_{\vec{X}} P(t; \vec{X}) - P(t; \vec{X}) F(\vec{X})], \quad \vec{X} \in \Omega^{N_C}, t > 0,$$

where  $\nabla_{\vec{X}} \cdot$  denotes the divergence operator with respect to  $\vec{X}$  and  $\nabla_{\vec{X}}$  is the corresponding gradient.

The Fokker-Planck equation is just as fundamental as the diffusion equation, because it provides a deterministic description of the evolution of the probability density for a stochastic system, enabling the analysis of macroscopic behaviour — such as diffusion, drift, and pattern formation — from microscopic particle dynamics.

It is derived using the continuity equation (or conservation of probability), which states that the rate of change of probability in a region is equal to the net flux of probability across its boundary, similarly to the model before.

This leads to a flux expression involving both advective (drift) and diffusive components. The divergence theorem is applied in the  $2N_C$  dimensional configuration space  $\Omega^{N_C}$  to convert surface integrals into volume integrals. This is the step where the additional term comes from, yielding the final form of the Fokker-Planck equation.

To transition from the joint probability density function to the first marginal density function in the presence of external forces, we consider the evolution of the system at the macroscopic level by integrating out the degrees of freedom of all but one particle. This process, which is analogous to the case of pure Brownian motion, relies

on the symmetry of the system: since the particles are identical and non-interacting, the joint density is invariant under permutations of particle labels.

The first marginal of the point particle model with external forces and Brownian motion is given by

$$(1) \quad \frac{\partial \rho(t; \vec{x})}{\partial t} = D \Delta_{\vec{x}} \rho(t; \vec{x}) - \nabla_{\vec{x}} \cdot (f(\vec{x}) \rho(t; \vec{x})), \quad \vec{x} \in \Omega, \quad t > 0.$$

The structure of the resulting Equation (1) for  $\rho$  mirrors that derived in the absence of external forces, with the key difference being the inclusion of a drift term due to the external force field  $f(\mathbf{x})$ . This similarity in derivation underscores the robustness of the marginalisation procedure, which consistently reduces the high-dimensional dynamics to a one-particle description, regardless of whether the motion is driven solely by diffusion or by a combination of diffusion and drift.

### Hard sphere model

Next, we consider models that add a real size to the particles and introduce particle interactions. With the inclusion of a real size, the particles cannot overlap, resulting in exclusion effects. To account for this, we introduce a new interaction dynamic that ensures the particles do not overlap. This leads to a more complex and realistic model that captures the behaviour of particles with a real size and interactions.

We model particles as spherical in shape, with a diameter  $0 < \epsilon \ll 1$ . Since particles cannot overlap, the domain  $\Omega_\epsilon^{N_C} \subset \Omega^{N_C}$ , that encodes where each particle centre can be located, must exclude the areas where

$$\|\vec{x}_i - \vec{x}_j\|_2 \leq \epsilon, \quad 1 \leq i < j \leq N_C.$$

This is due to the fact that particles cannot occupy the same space simultaneously. How this kind of exclusion works is visualized in an one dimensional example in Figure 2.

To define the new domain, we first describe the set of illegal configurations as

$$\mathcal{B}_\epsilon = \{(\vec{x}_1, \dots, \vec{x}_{N_C})^T \in \Omega^{N_C} \mid \exists i \neq j : \|\vec{x}_i - \vec{x}_j\|_2 \leq \epsilon\}.$$

Then we can define the ‘hollow’ domain

$$(2) \quad \Omega_\epsilon^{N_C} = \Omega^{N_C} \setminus \mathcal{B}_\epsilon.$$

Figure 3 illustrates how a hard sphere cell configuration looks like compared to a point particle configuration.

Under this circumstances, we will get a new dynamic compared to the point particle model. In the work of Bruna et al. [BC12], a hard sphere particle model is examined. All particles in this model are distinct and can be distinguished from one another. A diffusion constant,  $D > 0$ , is again included in the model to scale the Brownian motion.

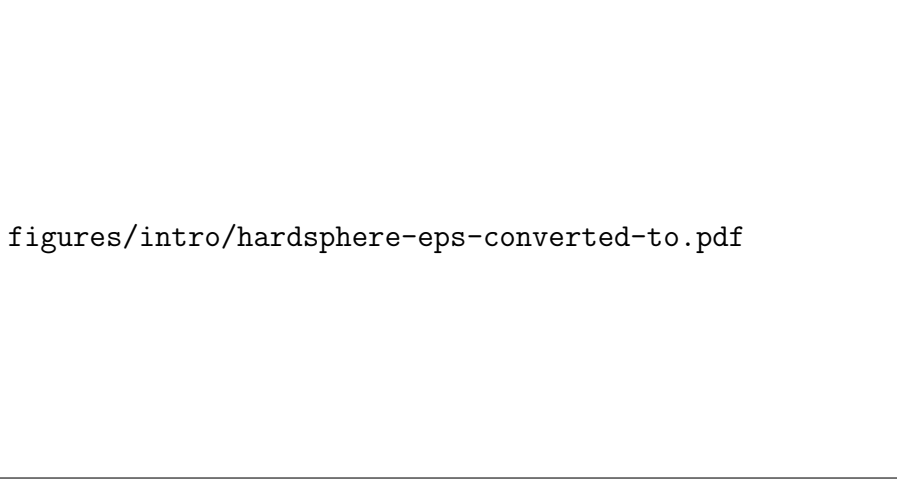
The dynamics of the particles are governed by the SDE

$$d\vec{x}_i(t) = f(\vec{x}_i(t)) dt + \sqrt{2D} d\vec{B}_i(t), \quad \vec{x}_i \in \Omega_\epsilon^{(i)}, \quad 1 \leq i \leq N_C,$$



`figures/intro/hardsphere_exclusion.png`

Figure 2: This plot illustrates the feasible regions for cell 2 in one dimensional space, dependent on the position of cell 1. The domain of interest is restricted to the one dimensional interval  $[-L, L]$ , with the two cells having a diameter of  $\epsilon$ . The red boundaries indicate the excluded regions, where neither cell can occupy a position closer than  $\frac{\epsilon}{2}$  to the boundary. The red diagonal line represents the occupied region by cell 1.



`figures/intro/hardsphere-eps-converted-to.pdf`

Figure 3: An illustration from [BC12] of the point particles on the left and the hard sphere particles on the right. We can see areas where the centre of the particles cannot be located, as they would overlap with other particles being marked red.

where  $\Omega_\epsilon^{(i)} \subset \Omega$  is the excluded volume domain for cell  $i$ , i.e.

$$\Omega_\epsilon^{(i)} = \{\vec{y} \in \Omega \mid \forall j \in \{1, \dots, N_C\} \setminus \{i\} : \|\vec{x}_j - \vec{y}\|_2 > \epsilon\}.$$

The particles are initially randomly distributed in  $\Omega_\epsilon^{N_C}$ , ensuring that no overlap occurs between the particles.

The dynamics of hard spheres share significant similarities with those of point particles, featuring both an external force  $f$  and Brownian motion. The primary difference lies in the constrained movement: hard spheres are confined to a domain that excludes the volume occupied by other spheres.

The model enforces this constraint using reflective boundary conditions on the collision surfaces whenever there are two cells with

$$\|\vec{x}_i - \vec{x}_j\|_2 = \epsilon, \quad 1 \leq i < j \leq N_C.$$

Due to the presence of numerous holes (occupied by other cells), these reflections create a unique dynamic where cells effectively bounce off each other, distinct from the unhindered motion of point particles.

Similarly as in the point particle model, we are now interested in the macroscopic view of this model. The structure for computing the first marginal of the hard sphere model is quite analogous to the computation for the point particles.

The joint probability density function  $P$  of the  $N_C$  particles satisfies the high dimensional Fokker-Planck equation

$$\frac{\partial P}{\partial t} = \nabla_{\vec{X}} \cdot [D \nabla_{\vec{X}} P - P F], \quad \vec{X} \in \Omega_{\epsilon}^{N_C}, \quad t > 0,$$

where  $\nabla_{\vec{X}}$  and  $\nabla_{\vec{X}} \cdot$  denote the gradient and divergence operators with respect to the  $N_C$  particle position vector  $\vec{X}$  and we again use  $F(\vec{X}) = (f(\vec{x}_1, \dots, f(\vec{x}_{N_C})))^T$ . The joint probability density function for hard spheres differs from that of point particles solely in its domain of definition. While the point particle model is defined on the full configuration space  $\Omega^{N_C}$ , the hard sphere model is governed by the same Fokker-Planck equation but restricted to the excluded volume domain  $\Omega_{\epsilon}^{N_C}$ . This domain restriction encodes the physical impenetrability of finite sized particles while preserving the mathematical structure of the evolution equation.

Using the method of matched asymptotic expansions, the authors also derived the probability density function  $\rho$  of finding a single particle at time  $t$  and position  $\vec{x}$ , which satisfies the equation

$$(3) \quad \begin{aligned} \frac{\partial \rho}{\partial t} &= \nabla_{\vec{x}} \cdot \{ D \nabla_{\vec{x}} [\rho + \frac{\pi}{2} (N_C - 1) \epsilon^2 \rho^2] - f \rho \} \\ &= D \Delta_{\vec{x}} \rho + D \frac{\pi}{2} (N_C - 1) \epsilon^2 \Delta_{\vec{x}} (\rho^2) - \nabla_{\vec{x}} \cdot (f \rho), \quad \vec{x} \in \Omega, \quad t > 0. \end{aligned}$$

Comparing Equation (3) (the first marginal distribution for hard spheres) with Equation (1) (the first marginal distribution for point particles), we observe an additional term in Equation (3). This term accounts for the enhanced diffusion rate resulting from the excluded volume effects of the hard spheres. As the particle diameter  $\epsilon \rightarrow 0$ , Equation (3) converges to Equation (1), recovering the dynamics of point particles.

It is important to note that while the joint probability density function for hard spheres is defined on the restricted configuration space  $\Omega_{\epsilon}^{N_C}$ , the first marginal density function  $\rho(t, \mathbf{x})$  remains defined on the original domain  $\Omega$ .

This distinction arises because  $\rho(t; \vec{x})$  is obtained by integrating the joint density

over all other particle positions, effectively averaging out the excluded-volume constraints.

For any position  $\vec{x} \in \Omega$ , there exist valid configurations where the first particle occupies  $\vec{x}$  while all other particles are positioned to avoid overlap. Consequently, the marginal density remains well defined across the entire domain  $\Omega$ , despite the joint density being restricted to  $\Omega_\epsilon^{N_C}$ .

In the derivation of Equation (3), the divergence theorem introduces additional boundary terms arising from the excluded volume holes in the configuration space  $\Omega_\epsilon^{N_C}$ . These boundary contributions, localized near particle-particle collision surfaces, ultimately generate the non linear diffusion correction term in the first marginal density equation for hard spheres. This term, proportional to the particle volume fraction, captures the excluded-volume effects that enhance collective diffusion compared to the point particle model. Bruna and Chapman [BC12] demonstrated that the excluded-volume effects of hard spheres lead to enhanced diffusion within the system. ■

This is also shown in Figure 7 from the original paper, which compares the diffusion behaviour of the point particle model and the hard sphere model. The figure confirms the enhanced diffusion behaviour of the hard sphere system, as the density profile exhibits greater spatial spreading across  $\Omega$  compared to the point particle model. It uses the Monte Carlo method for the point particles and the hard sphere in order to give a numerical approximation of the density dynamic. The Monte Carlo method involves running the simulation many times ( $M = 10000$ ). For each discrete subsquare of our domain, we count how many particles were found at that location across all runs at time  $t = 0.05$ . We then divide by the total number of runs to get the estimated probability density at that place and time. This estimated density converges to the true density as the number of runs increases.

### Soft sphere model

Next, we consider an extension of the model by introducing deformable soft spherical particles. This new model incorporates the effect of deformation and interaction between particles through a potential energy function that depends on the distance between the particles. E.g. the paper [BCR17], written by Bruna, Chapman and Robinson, analyses the diffusion properties of such a model.

The hard sphere model enforces rigid, non deformable cell boundaries through reflective boundary conditions at a fixed separation distance, leading to abrupt, instantaneous collisions without any interface deformation.

Cells are still represented solely by their centre points  $\vec{x}_i \in \Omega$ ,  $1 \leq i \leq N_C$ . Consequently, this model does not account for shape deformations, as no explicit cell boundary is included in the system.

In contrast to the hard sphere model, the soft sphere model does not enforce rigid reflective boundaries. Instead, it allows the centres of two cells to temporarily approach each other to a distance less than  $\epsilon$ . The system is driven to resolve such overlaps through a repulsive interaction potential,  $u : \mathbb{R}_+ \rightarrow \mathbb{R}$  that assigns an energy penalisation for a given intercellular distance. For repulsive short range potentials,  $u$  is characterised by a rapid decay from a high value at small separations to zero at larger distances.

The transition from reflective boundary conditions on neighbouring cell walls to interaction potentials renders the use of a hollow domain impractical. Therefore, we return to the original domain  $\Omega$ , within which all cells are located.

There are different approaches for modelling a specific function for  $u$ , that of course also change the cell system dynamics. The interaction potentials discussed in Bruna, Chapman, and Robinson [BC12], represent the energy of interaction between two particles separated by distance  $r$ . The cell diameter  $\epsilon > 0$  used in the hard sphere model now represents the range of interaction in the soft sphere setting. Nevertheless, it can still be interpreted as an effective cell diameter, since regions with  $r = \epsilon$  mark the transition between overlapping and non overlapping cells.

The simplest repulsive pair potential is the soft sphere (SS) potential, which assumes the form

$$u_{\text{SS}}(r) = \left(\frac{\epsilon}{r}\right)^\nu,$$

where  $\nu > 0$  is the hardness parameter that controls the steepness of the potential. As  $\nu$  increases, the potential becomes more hard sphere like, with the hard sphere limit ( $u(r) = \infty$  for  $r \leq \epsilon$  and  $u(r) = 0$  for  $r > \epsilon$ ) approached as  $\nu \rightarrow \infty$ .

Another common form is the exponential (EX) potential

$$u_{\text{EX}}(r) = e^{-r/\epsilon},$$

which features a smooth, rapidly decaying repulsion.

Once an interaction potential has been chosen, the dynamics of the soft sphere cell model for cell  $i$  can be defined as follows

$$d\vec{x}_i(t) = f(\vec{x}_i(t)) dt - \sum_{j \neq i} \nabla_{\vec{x}_i} u(\|\vec{x}_i(t) - \vec{x}_j(t)\|_2) dt + \sqrt{2D} d\vec{B}_i(t),$$

for  $1 \leq i \leq N_C$  and  $t > 0$ .

The authors derive the joint probability density for the soft sphere system as part of their many-particle Fokker-Planck formulation. They begin from the stochastic Langevin dynamics for  $N_C$  interacting particles subject to pairwise soft repulsive potentials, and then obtain the corresponding Fokker-Planck equation governing the evolution of the joint probability density as

$$\frac{\partial P}{\partial t} = \nabla_{\vec{X}} \cdot [D \nabla_{\vec{X}} P + P \nabla_{\vec{X}} \Phi], \quad \vec{X} \in \Omega^{N_C}, \quad t > 0,$$

where

$$\begin{aligned} \Phi : \Omega^{N_C} &\longrightarrow \mathbb{R}, \\ \vec{X} &\longmapsto \Phi(\vec{X}) = \sum_{i \neq j} u\left(\frac{\|\vec{x}_i - \vec{x}_j\|_2}{\epsilon}\right), \end{aligned}$$

is total interaction potential energy of the  $N_C$  particle system.

The authors continued by deriving the first marginal function, by integrating the joint probability density function of all particles over the positions of all other particles. They then used matched asymptotic expansions to obtain a closed equation for the first marginal, which is a non linear advection diffusion equation, given by

$$(4) \quad \frac{\partial \rho}{\partial t} = D \Delta_{\vec{x}} \rho - \nabla_{\vec{x}} \cdot (\rho f) + \nabla_{\vec{x}} \cdot (\alpha_u \epsilon^2 (N_C - 1) \rho \nabla_{\vec{x}} \rho), \quad \vec{x} \in \Omega, t > 0,$$

where  $\alpha_u$  depends on the interaction potential  $u$  and  $0 < \epsilon \ll 1$  is the interaction range of the particles. Crucially, the parameter

$$\alpha_u = \int_{\Omega} 1 - e^{-u(\epsilon \|x\|)} dx,$$

quantifies the strength of the non linear diffusion effect, with larger values corresponding to stronger excluded-volume effects that enhance the overall diffusion rate of the system.

When comparing the first marginals of the soft sphere model Equation (4) and the hard sphere model Equation (3), we can see that they are similar in structure, with the difference being the coefficients of the non linear diffusion terms. We can not clearly say which model diffuses faster, as this is dependent on the modelling of the soft interaction.

The influence of the cell hardness to the diffusion rate of the cell system will be investigated in this thesis. We even introduce a parameter that can continuously change the cell hardness from hard to soft.

While these models are powerful, they are limited to spherical particles and do not account for the complex shapes and deformations observed in biological cells.

## Phase field model

A new cell modelling framework is now considered which, unlike the models before, features cell deformation. The representation of a cell shifts from just a two dimensional point  $\vec{x}_i(t) \in \Omega$  to a phase field variable  $\phi_i(t, \vec{x}) : \mathbb{R}_+ \times \Omega \longrightarrow [-1, 1]$  that defines its cell border through the level null set, i.e., points  $\vec{x} \in \Omega$  where  $\phi_i(t, \vec{x}) = 0$ . The phase field approach exhibits conceptual parallels with the soft sphere model proposed by Bruna, Chapman, and Robinson [BCR17], particularly in how cell-cell interactions are modelled through a continuous repulsive energy that prevents overlap.

In both formulations, interactions are governed by a smooth, short range influence. The soft sphere model derives its interaction dynamics from the potential energy  $u(\|\vec{x}_i - \vec{x}_j\|_2)$ , which leads to a non linear diffusion equation featuring a diffusion coefficient that depends on local density.

The phase field model resolves cell overlaps through a free energy producing a repulsive force between cells. This enables gradual, continuous deformation of cell interfaces, thereby avoiding discontinuities in the dynamics that are characteristic of discrete collision models. Thus, the interaction mechanisms operate continuously and locally, ensuring a seamless transition between overlapping and non overlapping configurations while maintaining physical consistency in both models.

Nevertheless, the phase field model diverges fundamentally in its underlying structure: it is a continuum model based on partial differential equations that explicitly

encodes cell morphology and internal organisation through the phase field variable  $\phi_i$ , enabling dynamic shape changes, topological transitions, and coupling to geometric features such as surface curvature.

The free energy functional encodes shape regularization, intercellular interactions, and physical constraints of the system. Unlike the soft sphere model, which treats cells as point-like entities interacting via a smooth potential, the phase field model represents cells as much more complex, spatially extended, continuously structured entities, with their internal state fully described by the evolution of the phase field variable  $\phi_i$ . This enables a natural description of complex cell morphologies, topological transitions such as cell division or fusion, and the integration of cell mechanics with geometric curvature via extrinsic curvature contributions in the free energy.

Phase field variables represent cells as smooth functions  $\phi_i(\vec{x}, t) \in [-1, 1]$ , with  $\phi_i > 0$  in the cell interior and  $\phi_i < 0$  in the exterior. The cell wall is denoted by values of  $\phi_i = 0$ . An illustration of a phase field variable is shown in Figure 4.

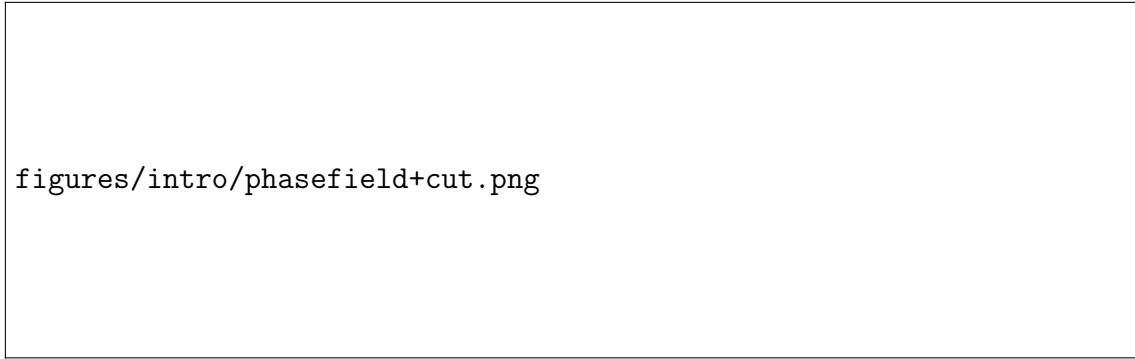


Figure 4: A snapshot from the paper [AT20] illustrating a phase field variable. The cell's inside has value  $\phi = 1$  and the outside  $\phi = -1$ . On the right, we can see a cut of the plot from the left. It also shows the cell wall level set with a dotted line.

The dynamics of a phase field variable  $\phi_i$  can typically be given by a gradient flow of a free energy functional:

$$\frac{\partial \phi_i}{\partial t} + v_0(\vec{v}_i \cdot \nabla_{\vec{x}} \phi_i) = \Delta_{\vec{x}} \frac{\delta F}{\delta \phi_i}, \quad 1 \leq i \leq N_C$$

where  $\vec{v}_i$  is a vector field used to incorporate activity, with a self propulsion strength  $v_0$ ,  $F$  is a free energy, and  $\frac{\delta F}{\delta \phi_i}$  denotes the first variation.

The free energy  $F$  arises from a sum of different energies,

$$F = F_{CH} + F_{INT} + F_M.$$

The first energy is a Cahn-Hilliard energy and could look like in [WV21]

$$F_{CH} = \sum_{i=1}^N \int_{\Omega} \frac{1}{Ca} \left( \frac{\epsilon}{2} \|\nabla_{\vec{x}} \phi_i\|_2^2 + \frac{1}{\epsilon} W(\phi_i) \right) d\vec{x},$$

where now,  $\epsilon$  is a small parameter related to the interface thickness, and  $Ca$  is a capillary number that scales the relative importance of surface tension. The term  $\|\nabla_{\vec{x}}\phi_i\|_2^2$  penalises a long cell wall, as  $\nabla_{\vec{x}}\phi_i \neq 0$  only at the cell wall. Thus, the Cahn-Hilliard energy always tries to minimize the area of the cell interface.

$W(\phi_i) = \frac{1}{4}(\phi_i^2 - 1)^2$  is a double-well potential. This energy ensures that each  $\phi_i$  maintains a stable interface of  $[-1, 1]$ .

The second energy term  $F_{INT}$  models cell-cell interactions and could be defined as in [WV21]

$$F_{INT} = \sum_{i=1}^N \frac{1}{Ca} \int_{\Omega} B(\phi_i) \sum_{j \neq i} w(d_j) d\vec{x},$$

where

$$B(\phi_i) = \frac{3}{4\sqrt{2}\epsilon} (\phi_i^2 - 1)^2$$

is an approximation of the delta function of the cell boundary that is non-zero only at the cell wall. The sum in the integral accounts for the interaction with all other cells  $j \neq i$  through a short-range potential  $w(d_j)$ , where  $d_j$  is the signed distance function to the cell boundary of cell  $j$ . When employing this dynamics, the interaction force  $F_{INT}$ , acts to reduce or eliminate cell overlaps.

The third energy term  $F_M$  differs for different models and incorporates additional mechanical properties of the cells, such as area conservation or bending energy. This energy is dependent on the use case of the model.

It can have a big influence on the dynamic of a phase field model, as analysed in [WV21], where the authors focussed on the influence of microscopic details to incorporate active forces on emerging phenomena.

Four different approaches are considered. One in which the activity is determined by a random orientation, one where the activity is related to the deformation of the cells, and two models with subcellular details to resolve the mechanical interactions underlying cell migration.

The random model determines the direction of motion on the single cell level by a stochastic process. The second model is called elongation model. It identifies the longest axis of the cell's phase field and aligns the direction of motion with this axis. The third and fourth models presented are referred to as the polar model and the nematic model, respectively. Cell motion strength and direction are determined based on subcellular details at the single-cell level.

All models are compared with respect to generic features, such as coordination number distribution, cell shape variability, emerging nematic properties, as well as vorticity correlations and flow patterns in large confluent monolayers and confinements. We can see the results in Table 1.

The goal of this paper is a systematic comparison of these approaches and their linkage with statistical observables of experiments to provide a route towards predictive simulations of patterns and correlations in cell colonies. Model predictions are compared with experimental data from various cell cultures. The qualitative differences observed highlight the importance of microscopic details.

characteristic	Random	Elongation	Polar	Nematic
Coordination number distribution	(✓)	(✓)	(✓)	(✓)
Shape variability	(✓)	✓	✓	(✓)
Rosette ratio	Differences between models			
Velocity distribution of topological defects	Differences between models			
Correlation between direction of motion and orientation of defect	✗	✓	✓	(✓)
Elastic property of + 12 defect	✗	Extensile	Contractile	Contractile
Active turbulence	(✓)	(✓)	(✓)	(✓)
Vorticity-vorticity correlation	Similar for all models			
Dependency of defect density on activity	Linear	Linear	Linear	Constant
Rotational motion in circular confinement	✗	(✓)	✗	✗

Table 1: Comparison of the four different phase field models from [WV21] with respect to various characteristics observed in experiments. A check mark ✓ indicates observed agreement, ✗ indicates disagreement and (✓) indicates only qualitative agreement with universal feature. If experimental data are not available or insufficient for a comparison, only similarities or differences of the models are noted.

A related study by Happel and Voigt [HV23] employs phase field models to investigate cell dynamics, specifically focusing on the influence of curved domains (defined as tori) on collective cell behaviour. The visualization of cells on a torus is shown in Figure 5.

Their work examines emergent phenomena like coordinated rotation on curved surfaces, driven by curvature alignment and self-propulsion. Unlike the soft sphere model, which typically assumes spherical symmetry and isotropic interactions, the

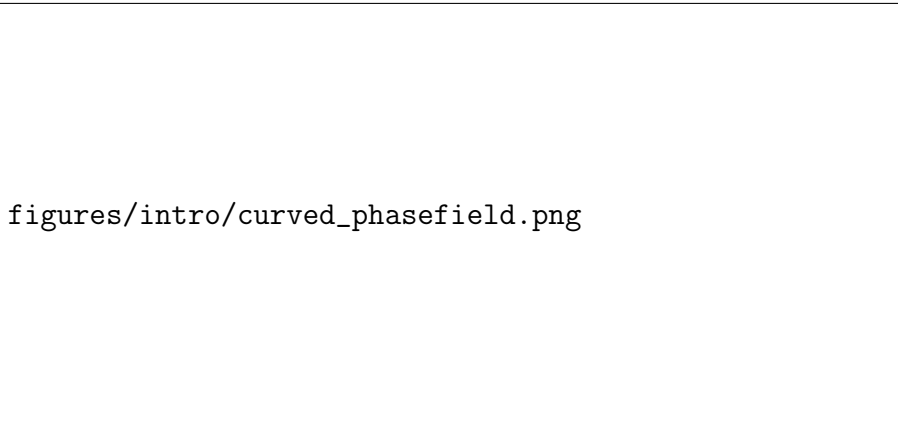


Figure 5: A figure from the paper [HV23] showing a phase field variable  $\phi$  on a curved domain, specifically a torus. In (a) and (b), the surface of the torus from (c) is shown as a parametrization on a rectangle, where the blue edges are identified (glued together) to form the toroidal direction, and the red edges are similarly identified to form the poloidal direction. Red and blue lines represent periodic boundary conditions, which are enforced by gluing the corresponding edges in (b) and (c). The color coding corresponds to the extrinsic curvature parameter  $E_c$  (see Eq. (3)):  $E_c = 0$  (purple) results in a geodesic circle on both geometries;  $E_c > 0$  (green) favours alignment with the direction of maximum absolute curvature;  $E_c < 0$  (yellow) favours alignment with the direction of minimal absolute curvature. Cell elongation is highlighted for visibility. On toroidal surfaces, cell shape depends on position due to varying curvature. (c) shows the trajectories, final positions, and shapes of cells over time. The influence of extrinsic curvature is not apparent in the final configuration, as all shapes were obtained by solving Eq. (1) with  $v_0 = 0$ .

phase field approach allows for the incorporation of anisotropic effects, such as alignment with principal curvature directions, through geometric coupling terms. This capability enables the simulation of complex collective behaviours but also increases computational demands compared to simpler point-particle models.

The phase field model developed by Happel and Voigt [HV23] highlights the critical role of extrinsic curvature coupling in dictating the alignment of cell elongation with principal curvature directions and the emergence of coordinated rotation in epithelial layers on curved surfaces. By combining a diffuse interface representation with a free energy incorporating both intrinsic and extrinsic geometric terms, their simulations successfully reproduce key experimental observations, including spontaneous rotation on cylindrical surfaces and curvature-dependent morphological changes on tori. This work emphasizes the significance of geometric constraints in tissue morphogenesis and offers a framework for investigating how curvature influences collective cell dynamics beyond planar environments.

### Vertex model

The last cell model approach is also the approach we choose in this thesis. Vertex models represent a powerful and versatile approach for simulating the mechanical behaviour of biological cells and tissues.

Originating from materials science and solid mechanics, these models represent cells as polygons, where the boundaries are defined by a discrete set of vertices connected by edges. The degrees of freedom in these models are precisely these vertices, meaning that all the cell model dynamics are applied only to the vertices.

The cell dynamic in a vertex model is usually given by the equation

$$(5) \quad \frac{d\vec{x}_i}{dt} = F_i^m,$$

where  $F_i^m$  is the total force acting on vertex  $1 \leq i \leq N_V$  of cell  $1 \leq m \leq N_C$ .

Like in the phase field model,  $F_i^m$  is a sum of different forces that define the cell behaviour, such as the cell flexibility or the interaction with other cells. The forces participating in  $F_i^m$  are often found as negative gradients of energies that shall be minimized. This method called gradient flow is also used for phase field models.

Due to their discrete nature, vertex models are computationally efficient compared to continuum models, while still providing rich insights into the interplay between cell mechanics and collective behaviour, making them invaluable for understanding fundamental principles governing cell organization and tissue dynamics across diverse biological contexts.

This geometric representation allows for the incorporation of key cellular properties, such as surface tension, cortical tension, adhesion, and local shape constraints, into an energy functional. Minimizing this energy through computational simulation enables the capture of emergent phenomena like tissue morphogenesis, cell migration, wound healing, and pattern formation.

The paper [FOBS14] developed a sophisticated vertex based model to simulate the dynamic behaviour of confluent epithelial cell sheets, representing tissues where cells completely cover the available space without gaps. Their model aims to capture key biological processes observed in real epithelial tissues.

Conservation of cell area and perimeter ensures cells maintain their size and shape during deformation. Junctional rearrangements, including neighbour exchange and vertex/edge merging, enable cell migration and tissue remodelling. Cell division is modelled by creating a rosette structure from multiple adjacent vertices and cell growth and death simulate changes in individual cell size. A detailed exploration of the implementation and specific consequences of these confluent specific mechanics is beyond the scope of this work. While these mechanisms are essential for understanding the complex dynamics of confluent tissues, the focus of this thesis lies on non confluent cell models, where the presence of interstitial space and variable packing density leads to distinct physical behaviours.

Boromand, Merkel, and Manning [BSY<sup>+</sup>18] investigated the jamming transition in a system of deformable cells using a vertex model. Of particular interest is their development of a non confluent cell model meaning that gaps between the cells are allowed by the model. This model is versatile and can be applied to simulate cells, foams, emulsions, and other soft particulate materials.

It uniquely combines the ability to represent individual deformable particles with the established shape energy function of the vertex model. This shape energy function incorporates terms that penalize deviations from a target area ( $a$ ) and perimeter

( $p$ ), along with repulsive interparticular forces to prevent overlap.

The model defines polygons with  $N_V \in \mathbb{N}$  vertices, where the bond vector  $\vec{l}_{mi}$  connects vertex  $\vec{v}_{m,i}$  to  $\vec{v}_{m,i+1}$ , i.e. vertex  $i$  to vertex  $i+1$  of cell  $m$ . The complete shape energy function, which governs the particle dynamics, integrates these various contributions:

$$E = E_{\text{contract}} + E_{\text{compress}} + E_{\text{line tension}} + E_{\text{bending}} + E_{\text{interaction}}.$$

The first energy reads

$$E_{\text{contract}} = \frac{k_l N_V}{2} \sum_{m=1}^{N_C} \sum_{i=1}^{N_V} (l_{m,i} - l_0)^2,$$

where  $k_l$  is the spring constant and  $l_0$  is the equilibrium length of the edges. It penalises contractions or expansion of cell edges and makes the edges return to their desired length  $l_0$ .

Similarly, the second force  $E_{\text{compress}}$  stabilises the cells area to a equilibrium area  $a_0$

$$E_{\text{compress}} = \frac{k_a}{2} \sum_{m=1}^{N_C} (a_m - a_0)^2,$$

where  $k_a$  is compressibility constant.

The line tension energy is another energy working with the cell edges. It sanctions long edges with the formula

$$E_{\text{line tension}} = \gamma \sum_{m=1}^{N_C} \sum_{i=1}^{N_V} l_{m,i},$$

where  $\gamma$  is the line tension coefficient.

The last shape energy is given by the bending energy. It acts to resist changes in the angles between adjacent edges of the polygonal cells. This energy encourages the cells to maintain smooth, relatively straight boundaries and discourages sharp bends or kinks.

$$E_{\text{bending}} = \frac{k_b}{2N_V} \sum_{m=1}^{N_C} \sum_{i=1}^{N_V} \left( \frac{2(\hat{l}_{m,i} - \hat{l}_{m,i+1})}{l_{m,i} - l_{m,i+1}} \right)^2,$$

where  $k_b$  is the bending rigidity constant,  $\hat{l}_{m,i} = \frac{\vec{l}_{m,i}}{\|\vec{l}_{m,i}\|_2}$  is the unit vector of  $\vec{l}_{m,i}$ . These four energies are conserving a specific cell shape.

There are two different methods to model the repulsive interaction between two deformable polygons called rough surface (RS) and smooth surface (SS) method. Both methods are illustrated in Figure 6.

In the Rough Surface (RS) method, the discrete nature of the polygonal cell representation is emphasized. Each vertex of a cell is treated as the center of a rigid disk with a fixed diameter, set to  $\delta = l_0$  (equilibrium bond length). Repulsive interactions between cells are then modelled as linear spring forces that arise when these

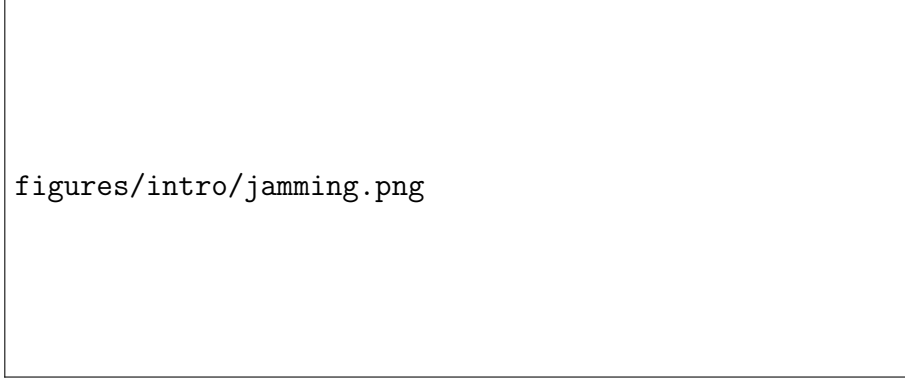


Figure 6: A snapshot from the paper [BSY<sup>+</sup>18] illustrating a configuration of vertex-based deformable cells. Schematic of deformable polygons with  $N_V = 34$  vertices (where the position of the  $j$ -th vertex in the  $m$ -th polygon is denoted by  $\vec{v}_{m,j}$ ), area  $a_m$ , and perimeter  $p_m$ . The edge  $l_{m,j} = p_m/N_V$  represents the line segment connecting vertices  $j$  and  $j + 1$  in polygon  $m$ . Two methods are used to model the edges of deformable polygons: (a) and (b) show the RS method, where disks of diameter  $\delta$  are centred at the polygon vertices; (c) and (d) show the SS method, where polygon edges are modelled as circulo-lines of width  $\delta$ . The quantity  $d_{\min}$  denotes the minimum distance between the line segments  $l_{m,j}$  and  $l_{n,k}$ .

disks overlap. This approach effectively simulates a rough surface interaction, characterized by discrete points of repulsion localized at the cell vertices, rather than a continuous interaction across the cell boundary.

$$E_{\text{RS}} = \sum_{m=1}^{N_C} \sum_{n>m}^N \sum_{j=1}^{N_V} \sum_{k=1}^{N_V} \frac{k_r}{2} (\delta - |\vec{v}_{m,j} - \vec{v}_{n,k}|)^2 \times \Theta(\delta - |\vec{v}_{m,j} - \vec{v}_{n,k}|),$$

where  $k_r$  is the repulsive constant and  $\Theta$  is the Heaviside step function, that is either 1 for a positive argument or 0 otherwise.

In contrast to the RS method, the Smooth Surface (SS) method adopts a smoother representation, modelling polygon edges as circulo-lines, essentially line segments with a finite width  $\delta$ . Repulsive forces are then calculated based on the minimum distance  $d_{\min}$ , between these circulo-line segments belonging to different polygons. The interaction energy is then formulated using this minimum distance  $d_{\min}$ .

$$E_{\text{SS}} = \sum_{m=1}^{N_C} \sum_{n \neq m}^N \sum_{j=1}^{N_V} \sum_{k=1}^{N_V} \frac{1}{2} k_r (\delta - d_{\min})^2 \Theta(\delta - d_{\min}).$$

This method provides a smoother, more continuous repulsion, better approximating the behaviour of soft, continuous interfaces.

Despite the different interaction mechanisms, both methods yield similar structural and mechanical properties at jamming onset. This indicates that the overall jamming behaviour is robust to the specific choice of interaction model.

### Discrete Form model

This thesis introduces the Discrete Form (DF) cell model, a vertex based framework

inspired by [FOBS14, BSY<sup>+</sup>18] for simulating cell dynamics in non-confluent systems, similar to [BSY<sup>+</sup>18], but typically using fewer vertices (e.g.,  $N_V = 6$ ).

The DF model incorporates shape preserving forces (area, edge, interior angle energies) and interaction forces (deforming and bounce overlap forces) derived as gradient flows of energy functionals, allowing for cell deformation like in [BSY<sup>+</sup>18, FOBS14, WV21, HV23] and ensuring evolution towards lower-energy configurations. This allows representation of a wide range of desired cell shapes.

The core contribution of this thesis is a non confluent DF model that systematically investigates how cellular deformability, controlled by a hardness parameter  $h \in [0, 1]$ , influences the overall diffusivity of the cell system, enabling a transition from hard disc like to soft disc-like behaviour.

## 1.2 Thesis overview

Building upon the foundations laid in the Bachelor’s thesis [Vog23], significant improvements were made, including bug fixes, code parallelization, and reformulation of forces for stable large-scale simulations (detailed in Sections ?? and ??).

Chapter 2 presents a rigorous validation by recreating the diffusion dynamics of the point particle and hard sphere models from [BC12] through extensive Monte Carlo simulations with varying hardness ( $h \in \{0, 0.5, 1\}$ ), representing soft, intermediate, and hard cell behaviours.

Subsequently, Chapter 3 analyses the resulting density dynamics. By connecting to the frameworks of [BC12, BCR17, BSY<sup>+</sup>18], this work provides a unified perspective on cell dynamics spanning rigid to deformable regimes. Finally, the thesis concludes with a summary of findings and an outlook on potential future extensions and applications of the DF model.

## 2 DF model validation and simulation analysis

- we continue by making cell simulations with the DF model.
- All of our simulations run in the Julia programming language. There, we used the package ‘DifferentialEquations.jl’ with its structure ‘SDEProblem()’ and then solved it with the package inbuilt Euler Maruyama scheme that uses a constant time step size.
- in order to place our simulations to existing papers, we aim to compare our simulation results to outcomes from an established cell model from [BC12].

### 2.1 Reference simulations: Bruna and Chapman (2012)

- The point particle and hard sphere models from [BC12] were already introduced in the Introduction 1.
- We will write down the explicit cell dynamics and first marginals again with all parameters applied. - The paper [BC12] analyses these dynamics on the domain

$$\Omega_{BC} = [-0.5, 0.5]^2,$$

on which  $N_C = 400$  particles are located.

- The point particle dynamic is given by

$$d\vec{x}_i(t) = \sqrt{2} d\vec{B}_i(t), \quad \vec{x}_i \in \Omega_{BC}^\circ,$$

for  $1 \leq i \leq N_C$ , where

$$\Omega_{BC}^\circ = (-0.5, 0.5)^2$$

denotes the interior of the domain  $\Omega_{BC}$ . We impose the reflective boundary condition on the boundary  $\partial\Omega$ .

Equation (1) shows the general first marginal of the point particle model. In our case, we choose the diffusion coefficient to be  $D = 1$  and we do not use an external force field, i.e.  $f(\vec{x}) = 0$ . Thus, the first marginal simplifies to

$$(6) \quad \frac{\partial \rho(t; \vec{x})}{\partial t} = \nabla_{\vec{x}} \cdot \nabla_{\vec{x}} \rho(t; \vec{x}), \quad \vec{x} \in \Omega, \quad t > 0,$$

which is expressed in divergence form.

- In order to transition to the hard sphere cell model, we introduce the cell diameter  $0 < \epsilon \ll 1$ .
- We recall from the Introduction 1 that the hard sphere dynamic is given by

$$d\vec{x}_i(t) = \sqrt{2} d\vec{B}_i(t), \quad \vec{x}_i \in \Omega_{BC,\epsilon}^\circ,$$

where we again choose  $D = 1$  and  $f(\vec{x}) = 0$ .

- Note, that we are now working on the excluded volume domain  $\Omega_{BC,\epsilon}$ , defined in Equation (2) that excludes areas where two cells would overlap.
- This domain has a more complex boundary  $\partial\Omega_{BC,\epsilon}$  that includes both the outer

boundary of the domain  $\Omega_{BC}$  and inner boundaries where two cells touch each other.

- Thus, we have much more reflections than in the point particle model, caused by the reflective boundary condition.

- When computing the first marginal of the hard sphere model, we get Equation (3). In our case, this simplifies to

$$(7) \quad \frac{\partial \rho}{\partial t} = \nabla_{\vec{x}} \cdot \nabla_{\vec{x}} [\rho + \frac{\pi}{2}(N_C - 1)\epsilon^2\rho^2], \quad \vec{x} \in \Omega, t > 0.$$

The initial condition of both models follows a two dimensional normal distribution with the addition that the distance of each cell centre to all others is at least  $\epsilon$ . The used distribution  $\mathcal{N}_2(0, 0.09^2 \cdot I_2)$  has an integral of one over  $\Omega_{BC}$ .

We can compute this initial condition with Algorithm 2.1. The avoidance of cell overlaps by the following algorithm is also illustrated in Figure 3.

- All codes were implemented in Julia [BEKS17]
- We used Distributions.jl [BPA<sup>+</sup>21] and its function ‘MvNormal()’ to generate the normal distributed points
- The Julia package [RN17] ‘DifferentialEquations.jl’ was used to solve the SDEs with its inbuilt Euler Maruyama scheme with static time step size.
- all self made plots in this thesis are created with Plots.jl [CSR<sup>+</sup>23].
- parallelisation of the monte carlo simulations was done with Julia built in ‘Distributed’ package [Wri23].

### **Algorithm 2.1. Computation of the initial cell system**

1. Generate a point  $\vec{x} \sim \mathcal{N}_2(0, 0.09^2 \cdot I_2)$ .
2. If for all already generated centres  $\vec{x}_j : \|\vec{x} - \vec{x}_j\|_2 > \epsilon$  is true, use  $\vec{x}$  as the next cell centre, otherwise discard the point and restart with step 1 until  $N_C$  cell centres are found.

The marginal equation (7) exhibits an enhanced diffusion rate because of the additional positive nonlinear term  $\frac{\pi}{2}(N_C - 1)\epsilon^2\rho^2$  inside the diffusion operator. This term represents excluded-volume interactions between finite-sized particles, which especially bias motion at regions of high density and thereby accelerate the overall spread. As a result, the effective collective diffusion increases with particle number  $N_C$ , particle size  $\epsilon$ , and local density  $\rho$ . We can rewrite Equation (7) to explicitly show this enhanced diffusion effect as follows:

$$\begin{aligned} \frac{\partial \rho}{\partial t} &= \nabla_{\vec{x}} \cdot \nabla_{\vec{x}} [\rho + \frac{\pi}{2}(N_C - 1)\epsilon^2\rho^2] \\ &= \nabla_{\vec{x}} \cdot [\nabla_{\vec{x}}\rho + \frac{\pi}{2}(N_C - 1)\epsilon^2\nabla_{\vec{x}}\rho^2] \\ &= \nabla_{\vec{x}} \cdot [\nabla_{\vec{x}}\rho + \frac{\pi}{2}(N_C - 1)\epsilon^22\rho\nabla_{\vec{x}}\rho] \\ &= \nabla_{\vec{x}} \cdot [\underbrace{(1 + \pi(N_C - 1)\epsilon^2\rho)}_{= D(\epsilon, N_C, \rho)} \nabla_{\vec{x}}\rho], \end{aligned}$$

where we used the product rule for gradients in the third line. Here,

$$D(\epsilon, N_C, \rho) = 1 + \pi(N_C - 1)\epsilon^2\rho$$

acts as an effective diffusion coefficient that depends on the particle size, total particle number, and local concentration. For  $\epsilon = 0$ , we recover Equation (6), corresponding to point particles with  $D = 1$  and for  $\epsilon > 0$ , we obtain Equation (7) as shown in the computation. This reformulation clearly demonstrates how excluded-volume interactions in the hard-sphere cell model lead to an enhanced diffusion rate compared to the point-particle case.



Figure 7: This figure from [BC12] contains the following four plots, all of them are shown at time  $t = 0.05$ . For all plots, the initial condition is normally distributed with mean  $(0, 0)^T$  and standard deviation 0.09. (a) shows the solution of the linear diffusion Equation (1) for point particles. (b) shows the histogram of a Monte Carlo simulation of the point particle model. (c) shows the solution of the non linear diffusion Equation (3) for finite-sized particles. (d) shows the histogram of a Monte Carlo simulation of the hard sphere model. The Monte Carlo simulations used  $10^4$  simulation runs each with a time step size of  $10^{-5}$ . We can see that the hard sphere model in (c) and (d) shows a quicker diffusion rate as the cell concentration in the centrum of the domain has already diffused more compared to the point particle model in (a) and (b).

Another evidence of this behaviour is shown in Figure 7 which is originally from the considered paper [BC12].

Here, we can see two Monte Carlo simulations. A Monte Carlo simulation, as for example described in [MU49] is a computational technique that uses random sampling to model and analyse complex systems or processes that are difficult to solve analytically. It repeatedly generates random inputs according to specified probability distributions and computes the resulting outcomes to estimate quantities like averages, variances, or distributions.

In our case, the Monte Carlo simulations are used to track the positions of cell centres over time. Each simulation begins from an initial configuration of cells, which is consistently generated using Algorithm 2.1. After initialization, the prescribed dynamics - either the point particle model or the hard sphere model - are applied, and the positions of the cell centres are recorded at a fixed time point,  $t = 0.05$ .

To visualise the results, we construct heatmaps representing the spatial distribution of cells at the final time. This is done by discretizing the domain into a uniform grid of sub squares. For each sub square, we count how many cells fall within it across all simulations. The resulting counts are normalised by dividing by the total number of cells  $N_C$ , the number of simulations, and the area of a sub square. This normalisation ensures that the heatmap represents a probability density, satisfying the mass conservation condition:

$$\sum_{i \in \text{sub squares}} \text{value}_i \cdot \text{area}_i = 1.$$

This approach provides a smooth estimate of the empirical cell density, allowing direct comparison with the corresponding solutions of the diffusion equations.

## 2.2 Reproduction of reference results

Before running our new dynamics that include cell flexibility, we first want to guarantee that the simulations are running in the correct setup. Therefore, we started with recreating the Monte Carlo simulation for the point particles. We always fixed the color scale to be the same as in [BC12] in order to gain comparability. The simulation parameters are the same as in [BC12].

Beside of this, all particles moved according to the two dimensional Brownian motion

$$d\vec{x}_i(t) = \sqrt{2} d\vec{B}_i(t), \quad 1 \leq i \leq N_C.$$

Figure ?? shows the evolution of the particle density in terms of heatmaps for different time steps. The results of our Monte Carlo simulation appear to be in good agreement with those of Bruna and Chapman, suggesting that our approach is robust and accurate.

Next, we consider the HSCM and run the Monte Carlo simulation for a cell diameter of  $\epsilon = 0.01$ . Figure 8 shows the density evolution of the HSCM.

## 2.3 Shape deformation check

In this subsection, we are going to investigate how much the cells deformed throughout our big monte carlo simulations. Therefore, we need to introduce a measure of

how much a cell is deformed. There is already some theory existing on how to measure that for two dimensional figures. A basic approach is to study the ratio between cell area and cell perimeter. We call that ratio the isoperimetric quotient  $\alpha$  of that geometric figure  $F$ , i.e.

$$\alpha_F = \nu \frac{\text{area}_F}{\text{perimeter}_F^2},$$

where  $\nu > 0$  is a scaling factor which we will define later.

There is one 2 dimensional geometric figure that has the largest isoperimetric quotient from all: the circle. For a circle of radius  $r > 0$ , we have a area of  $\text{area}_c = \pi r^2$  and a perimeter of  $\text{perimeter}_c = 2\pi r$ . Thus, it has an isoperimetric quotient of

$$\alpha_{circle} = \nu \frac{\pi r^2}{(2\pi r)^2} = \nu \frac{1}{4\pi}.$$

We want to normalise the isoperimetric quotient to always be in the interval  $[0, 1]$ . Therefore, we just have to choose  $\nu = 4\pi$ . Since a circle always has a maximum isoperimetric quotient, we have an upper bound of 1. It also has 0 as a lower bound since both the area and perimeter of a geometric figure are always positive.

These properties are also easy to compute for our DF cells. We can use the Shoelace Formula ?? for the cell area, and for getting the perimeter, we just have to add up the lengths of all cells.

We can use this approach to analyse how much our cell shapes changed in our big

Cell shape	Area	Perimeter	Asphericity
Triangle	$3.25 \times 10^{-5}$	0.0260	0.605
Square	$5.00 \times 10^{-5}$	0.0283	0.785
Hexagon	$6.50 \times 10^{-5}$	0.0300	0.907
Circle	$7.85 \times 10^{-5}$	0.0314	1.000

Table 2: Geometric properties of different DF cell shapes and a circle. The asphericity values increase with the number of vertices, approaching 1 as the shape becomes more circular. The target DF cell shape used in our Monte Carlo simulations has an asphericity of approximately  $\alpha \approx 0.907$ .



Figure 8: Heatmaps of a Monte Carlo simulation of the DF cell model with different hardness values at the times  $t \in \{0.00, 0.01, \dots, 0.05\}$ . Left column (*a*) shows hardness 0, we can see hardness 0.5 in the middle (*b*) and hardness 1 on the right (*c*). We can observe that the diffusion rate increases with increasing hardness.



Figure 9: This figure shows the evolution of the cross section density for our three Monte Carlo simulations at the sample times  $t \in \{0, 0.01, \dots, 0.05\}$ . Initially, each simulation starts with the same distribution. Note that the scaling of the  $y$ -axis changes from  $[0, 3.5]$  at  $t = 0$  to  $[0.7, 1.3]$  at  $t = 0.05$ , indicating diffusion in the density distribution for all hardnesses. As the plots show, the higher the hardness, the faster the diffusion for  $t > 0$ , since we observe a lower density in the middle ( $x = 0$ ) and a higher density near the interval borders for higher hardness values. Thus, the density distribution is already more even for higher hardnesses at  $t > 0$ .



Figure 10: Examples of DF cells and a circle illustrating their geometric properties. The DF cells are represented as regular polygons with  $N_V \in \{3, 4, 6\}$  vertices. For each case, the cell shape, area, perimeter and asphericity are shown in Table 2. The third DF cell with  $N_V = 6$  vertices corresponds to the target DF cell configuration used in our Monte Carlo simulations, exhibiting an asphericity of approximately  $\alpha \approx 0.907$ . As the number of vertices increases, the asphericity rises, reaching its maximum value of  $\alpha = 1.0$  for the circular case.



Figure 11: This figure illustrates how the cell asphericities change in the Monte Carlo simulations for hardnesses  $h \in \{0, 0.5, 1\}$ . Each simulation was performed with 400 cells, and 50 independent runs were conducted for each of the hard, mid, and soft simulation types. Initially, all cells are in their desired states, as shown in the third picture of Figure 10, having an asphericity of  $\alpha \approx 0.907$ . For  $h = 1$ , we can see that all 400 cells keep their standard asphericity of  $\alpha \approx 0.907$ , as no cell shape deformation is done in this setting. For the other two simulations, the asphericity values were  $\alpha \in [0.3, 0.92]$  for the soft model ( $h = 0$ ) and  $\alpha \in [0.84, 0.92]$  for the mid-hardness model ( $h = 0.5$ ). The full asphericity interval for the soft model is not shown for improved visualization. We observe that the largest shape deformations occur at the beginning of the simulation ( $t > 0$ ), when the most cell collisions happen in the crowded center. This is reflected by the increasing number of cell asphericities in the last interval  $[0.9, 0.92]$  over time for both the soft and mid-hardness simulations, if we exclude the initial state at  $t = 0$  where overlaps were prevented algorithmically.

### 3 Density computations

In the previous chapter, we studied Monte Carlo simulations of our DF model and visualised the resulting particle distributions as heatmaps at different time points. These simulations provided valuable insight into the statistical behavior of the system for finite numbers of cells.

In this chapter, we pursue a different approach: instead of extracting approximate density fields from stochastic simulations, we aim to compute the underlying density distribution function  $\rho$  that describes the limiting behavior of the system as the number of cells  $N_C \rightarrow \infty$ . More precisely, we seek the density  $\rho$  such that the limiting measure  $\mu$  satisfies  $d\mu = \rho(x)dx$ . Of course, this density will depend on the desired cell state, i.e. the number of vertices and its shape, as well as on the forces we apply on the vertices as the dynamic and their scalings.

As a starting point for this analytical treatment, we consider the empirical measure  $\mu^{N_C}$ , which encodes the particle configuration at finite  $N_C$ , and study its convergence to the continuous measure  $\mu$ .

The empirical measure  $\mu^{N_C} \in \mathcal{P}(\mathbb{R}^2)$  is the starting point of this computation.

Let  $\{\vec{x}_i\}_{i=1}^{N_C} \subset \mathbb{R}^2$  be the set of all cells' centre points. We define  $\mu^{N_C}$  as:

$$\begin{aligned}\mu^{N_C} : \mathcal{B}(\mathbb{R}^2) &\rightarrow [0, 1] \\ \mu^{N_C}(A) &= \frac{1}{N_C} \sum_{i=1}^{N_C} \delta_{\vec{x}_i(t)}(A),\end{aligned}$$

where  $\mathcal{B}(\mathbb{R}^2)$  is the Borel sigma-algebra on  $\mathbb{R}^2$  and  $\delta_{\vec{x}_i(t)}$  denotes the Dirac measure:

$$\begin{aligned}\delta_{\vec{x}_i(t)} : \mathcal{B}(\mathbb{R}^2) &\rightarrow \{0, 1\} \\ \delta_{\vec{x}_i(t)}(A) &= \begin{cases} 1 & \text{if } \vec{x}_i(t) \in A, \\ 0 & \text{if } \vec{x}_i(t) \notin A. \end{cases}\end{aligned}$$

For any test function  $\phi \in C_c^\infty(\mathbb{R}^2)$ , the Dirac measure satisfies

$$\int_{\mathbb{R}^2} \phi(x) d\delta_{\vec{x}_i(t)}(x) = \phi(\vec{x}_i(t)).$$

For a set  $A \in \mathcal{B}(\mathbb{R}^2)$ ,  $\mu^{N_C}(A)$  is the relative proportion of the  $N_C$  particles that are located in  $A$ .

For a finite  $N_C \in \mathbb{N}$ ,  $\mu^{N_C}$  is a discrete measure that only has its mass divided on the exact particle locations. As we increase the number of particles,  $\mu^{N_C}$  will spread out - having more particle locations to cover with each particle having a lower influence on the result of  $\mu^{N_C}$  as we divide through  $N_C$ . This process is quite similar to the transition from a sum to an according integral:

$$\sum_{i=1}^{N_C} \frac{1}{N_C} f(x_i) \xrightarrow{N \rightarrow \infty} \int f(x) dx,$$

where we can also see a transition from a discrete starting problem, having discrete points  $x_i$ , to a continuous integral where  $x \in (a, b)$ . As  $\mu^N$  is a measure that lives on

figures/density/muplot\_combined.png

Figure 12: Visualisation of empirical measures  $\mu^{N_C}$  for increasing numbers of cells, alongside the corresponding theoretical density. This visualisation illustrates the transition  $\mu^{N_C} \xrightarrow{N_C \rightarrow \infty} \mu$ .

All cell configurations are sampled from the same initial condition described in the previous chapter: a two-dimensional normal distribution  $\mathcal{N}_2((0, 0), \sigma^2 I_2)$  with  $\sigma = 0.09$ . In the first three subplots, the domain  $[-0.5, 0.5]^2$  is discretised into square bins of side length  $\frac{1}{50}$ . Each bin  $A$  corresponds to a measurable set in the definition of the empirical measure  $\mu^{N_C}(A) = \frac{1}{N_C} \sum_{i=1}^{N_C} \delta_{x_i}(A)$ , where the color intensity encodes the number of cells in that bin.

The first subplot shows a realisation with  $N_C = 20$  cells, the second with  $N_C = 200$ , and the third with  $N_C = 20.000$ . We observe that as  $N_C$  increases, the empirical measure  $\mu^{N_C}$  becomes a smoother approximation of the underlying density. The color scale is fixed across all subplots to allow direct visual comparison. The fourth panel displays the exact density function of the initial distribution,  $\rho(x) = \frac{1}{2\pi\sigma^2} \exp\left(-\frac{\|x\|^2}{2\sigma^2}\right)$ , with  $\sigma = 0.09$ .

sets  $A \in \mathcal{B}(\mathbb{R}^d)$ , we cannot directly plot it as a function. Instead, we try to visualise it meaningfully by using histograms as approximations in Figure 12. This is also a good connection from the previous section, where we also used histograms to show the results of the monte carlo simulations.

The distribution from the fourth subplot in Figure 12 is aimed to be computed for the dynamics of our DF cell model.

In the end, we want to achieve:

$$\mu^{N_C} \xrightarrow{N_C \rightarrow \infty} \mu$$

by letting the number of cells go to infinity.

### 3.1 Transition $\mu^{N_C} \xrightarrow{N_C \rightarrow \infty} \mu$

### 3.2 General energy computation

Lets define our cell centres with:

$$\vec{X} = (\vec{x}_1, \dots, \vec{x}_N) \in \mathbb{R}^{2N} \text{ (vector of all cell centres),}\\ \text{for } \vec{x}_i \in \mathbb{R}^2, 1 \leq i \leq N.$$

The energy that gets used for our cell dynamic shall be:

$$\begin{aligned} E : \mathbb{R}^2 &\rightarrow \mathbb{R} \\ E(\vec{x}_i) &= \frac{1}{2} |\vec{x}_i|^2. \\ \nabla_{(\vec{x}_i)} E(\vec{x}_i) : \mathbb{R}^2 &\rightarrow \mathbb{R}^2 \\ \nabla_{(\vec{x}_i)} E(\vec{x}_i) &= |\vec{x}_i|. \end{aligned}$$

We define the dynamic of a particle  $\vec{x}_i$  via:

$$\frac{d\vec{x}_i}{dt} = -\nabla_{\vec{x}_i} E(\vec{x}_i) \in \mathbb{R}^2.$$

We define the probability measure:

(question: is  $\mu$  defined on a single particle [ $\mu^{N_C} \in \mathcal{P}(\mathbb{R}^2)$ ] or on the whole particle system [ $\mu^{N_C} \in \mathcal{P}(\mathbb{R}^{2N})$ ])

(question: what does  $\mu$  say?

Its 1 when the particle is at a given location? vs Its 1 when the particle system is at a given configuration?)

$$\mu : \mathbb{R}^2 \rightarrow [0, \infty)$$

$\mu$  is the density of cell system.  $\mu^N$  is the empirical measure. It takes a subset  $A \subset \mathbb{R}^2$  as an argument and gives the relative number of particles that are inside of  $A$ .

Let  $\phi \in C_c^\infty(\mathbb{R}^2, \mathbb{R})$  (??) be a test function. Its gradient field is  $\nabla \phi : \mathbb{R}^2 \rightarrow \mathbb{R}^2$ . We compute:

$$\begin{aligned} \frac{d}{dt} \int \phi d\mu^N &= \frac{d}{dt} \left( \frac{1}{N_C} \sum_{i=1}^{N_C} \phi(\vec{x}_i) \right) \\ &= -\frac{1}{N_C} \sum_{i=1}^{N_C} \nabla \phi(\vec{x}_i) \cdot \nabla E(\vec{x}_i) \\ &= -\frac{1}{N_C} \sum_{i=1}^{N_C} \int \nabla \phi(x) \cdot \nabla E(x) d\delta_{\vec{x}_i} \\ &= - \int \nabla \phi(x) \cdot \nabla E(x) d\mu^N dx \\ &= \int \phi(x) \nabla \cdot (\mu^N(\nabla E(x))) dx \end{aligned}$$

$$\Rightarrow 0 = \partial_t \rho - \nabla(\rho_v),$$

where  $\rho$  is the density function of  $\mu$  such that

$$\mu(dx) = \rho(x) dx.$$

question: what is the space we integrate above? (i gues  $\mathbb{R}^{2N}$ )

## 4 Conclusion

In this work, we develop a vertex-based discrete form (DF) model that captures the behavior of deformable cells with realistic mechanical interactions, including shape preservation, cell-cell overlap resolution, and stochastic motion.

## 5 Outlook

An interesting extension of the current model would involve assigning individual desired states to each cell, in contrast to the uniform desired state used throughout this study. This modification would naturally lead to cell-specific energies and corresponding forces, as both would depend on the unique desired configuration of each cell. Incorporating such heterogeneity could allow the model to capture more complex biological behaviors, such as differentiation, cell-type-specific migration, or adaptive responses to environmental cues.

- incorporate external force  $f$ ,
- curved surfaces
- 3d
- cell division
- more parameter studies
- use more vertices
- limit  $N_V \rightarrow \infty$
- overdamping
- new shapes
- Additionally, many vertex models incorporate rules that govern changes in connection among vertices, and therefore allow for changes in cell neighbor relationships.
- These approximations are suitable in the case of tightly packed cell sheets, where the intercellular space is negligible, and is based on experimental observations that cells in epithelial tissues are often arranged in polygonal or polyhedral structures (19) and can move around relative to other cells (20)

## **Statement of authorship**

I hereby declare that I have written this thesis (*Derivation and study of a non-confluent model for deformable cells*) under the supervision of Jun.-Prof. Dr. Markus Schmidtchen independently and have listed all used sources and aids. I am submitting this thesis for the first time as part of an examination. I understand that attempted deceit will result in the failing grade „not sufficient“ (5.0).

---

Tim Vogel

Dresden, November 4, 2025

Technische Universität Dresden

Matriculation Number: 4930487

## References

- [AT20] Ricard Alert and Xavier Trepat. Physical models of collective cell migration. *Annual Review of Condensed Matter Physics*, 11(1):77–101, 2020.
- [BC12] Maria Bruna and S. Jonathan Chapman. Excluded-volume effects in the diffusion of hard spheres. *Phys. Rev. E*, 85:011103, Jan 2012.
- [BCR17] Maria Bruna, S. Jonathan Chapman, and Martin Robinson. Diffusion of particles with short-range interactions. *SIAM Journal on Applied Mathematics*, 77(6):2294–2316, 2017.
- [BEKS17] Jeff Bezanson, Alan Edelman, Stefan Karpinski, and Viral B Shah. Julia: A fresh approach to numerical computing. *SIAM Review*, 59(1):65–98, 2017.
- [BPA<sup>+</sup>21] Mathieu Besançon, Theodore Papamarkou, David Anthoff, Alex Arslan, Simon Byrne, Dahua Lin, and John Pearson. Distributions.jl: Definition and modeling of probability distributions in the julastats ecosystem. *Journal of Statistical Software*, 98(16):1–30, 2021.
- [BSY<sup>+</sup>18] Arman Boromand, Alexandra Signoriello, Fangfu Ye, Corey S. O’Hern, and Mark D. Shattuck. Jamming of deformable polygons. *Phys. Rev. Lett.*, 121:248003, Dec 2018.
- [CCP<sup>+</sup>14] Danfeng Cai, Shann-Ching Chen, Mohit Prasad, Li He, Xiaobo Wang, Valerie Choesmel-Cadamuro, Jessica K Sawyer, Gaudenz Danuser, and Denise J Montell. Mechanical feedback through e-cadherin promotes direction sensing during collective cell migration. *Cell*, 157(5):1146–1159, 2014.
- [CSR<sup>+</sup>23] Simon Christ, Daniel Schwabeneder, Christopher Rackauckas, Michael Krabbe Borregaard, and Thomas Breloff. Plots.jl – a user extendable plotting api for the julia programming language. 2023.
- [CV15] Andrew G Clark and Danijela Matic Vignjevic. Modes of cancer cell invasion and the role of the microenvironment. *Curr Opin Cell Biol*, 36(13-22):10–1016, 2015.
- [DRSB<sup>+</sup>05] Olivia Du Roure, Alexandre Saez, Axel Buguin, Robert H Austin, Philippe Chavrier, Pascal Siberzan, and Benoit Ladoux. Force mapping in epithelial cell migration. *Proceedings of the National Academy of Sciences*, 102(7):2390–2395, 2005.
- [FG09] Peter Friedl and Darren Gilmour. Collective cell migration in morphogenesis, regeneration and cancer. *Nature reviews Molecular cell biology*, 10(7):445–457, 2009.

- [FNW<sup>+</sup>95] Peter Friedl, Peter B Noble, Paul A Walton, Dale W Laird, Peter J Chauvin, Roger J Tabah, Martin Black, and Kurt S Zänker. Migration of coordinated cell clusters in mesenchymal and epithelial cancer explants in vitro. *Cancer research*, 55(20):4557–4560, 1995.
- [FOBS14] Alexander G. Fletcher, Miriam Osterfield, Ruth E. Baker, and Stanislav Y. Shvartsman. Vertex models of epithelial morphogenesis. *Biophysical Journal*, 106(11):2291–2304, 2014.
- [GT18] Matthew Good and Xavier Trepat. Cell parts to complex processes, from the bottom up, 2018.
- [Her32] Earl H Herrick. Mechanism of movement of epidermis, especially its melanophores, in wound healing, and behavior of skin grafts in frog tadpoles. *The Biological Bulletin*, 63(2):271–286, 1932.
- [Hol14] SJ Holmes. The behavior of the epidermis of amphibians when cultivated outside the body. *J. exp. Zool*, 17(2):281–295, 1914.
- [HV23] Lea Happel and Axel Voigt. Coordinated motion of epithelial layers on curved surfaces. *Cluster of Excellence, Physics of Life, TU Dresden*, 2023.
- [JGS18] Frank Jülicher, Stephan W Grill, and Guillaume Salbreux. Hydrodynamic theory of active matter. *Reports on Progress in Physics*, 81(7):076601, 2018.
- [MJR<sup>+</sup>13] M Cristina Marchetti, Jean-François Joanny, Sriram Ramaswamy, Tanniemola B Liverpool, Jacques Prost, Madan Rao, and R Aditi Simha. Hydrodynamics of soft active matter. *Reviews of modern physics*, 85(3):1143–1189, 2013.
- [MU49] Nicholas Metropolis and S. Ulam. The monte carlo method. *Journal of the American Statistical Association*, 44(247):335–341, 1949. PMID: 18139350.
- [PJJ15] Jacques Prost, Frank Jülicher, and Jean-François Joanny. Active gel physics. *Nature physics*, 11(2):111–117, 2015.
- [RCCT17] Pere Roca-Cusachs, Vito Conte, and Xavier Trepat. Quantifying forces in cell biology. *Nature cell biology*, 19(7):742–751, 2017.
- [RN17] Christopher Rackauckas and Qing Nie. Differentialequations.jl – a performant and feature-rich ecosystem for solving differential equations in julia. *The Journal of Open Research Software*, 5(1), 2017. Exported from <https://app.dimensions.ai> on 2019/05/05.
- [TWA<sup>+</sup>09] Xavier Trepat, Michael R Wasserman, Thomas E Angelini, Emil Millet, David A Weitz, James P Butler, and Jeffrey J Fredberg. Physical forces during collective cell migration. *Nature physics*, 5(6):426–430, 2009.

- [Vog23] Tim Vogel. Modelling of cells and their dynamics. 2023.
- [VT66] RB Vaughan and JP Trinkaus. Movements of epithelial cell sheets in vitro. *Journal of cell science*, 1(4):407–413, 1966.
- [Wri23] James Wrigley. Distributed.jl. 2023.
- [WV21] Dennis Wenzel and Axel Voigt. Multiphase field models for collective cell migration. *Physical Review E*, 104(5):054410, 2021.